

Article

Sources of Metallogenic Materials of the Saima Alkaline Rock-Hosted Niobium–Tantalum Deposit in the Liaoning Region: Evidence from the Sr-Nd-Pb and Li Isotopes

Yue Wu ¹, Nan Ju ^{1,2,*} , Xin Liu ¹, Lu Shi ¹, Yuhui Feng ³ and Danzhen Ma ²

¹ Shenyang Center of China Geological Survey, Shenyang 110034, China; wuyuemay005@163.com (Y.W.)
² School of Earth Sciences and Resources, China University of Geosciences (Beijing), Beijing 100083, China
³ College of Paleontology, Shenyang Normal University, Shenyang 110034, China
* Correspondence: junan@mail.cgs.gov.cn; Tel.: +86-181-04025767

Abstract: The Saima alkaline rock-hosted niobium–tantalum deposit (hereafter referred to as the Saima Deposit) is situated in the Liaodong Peninsula, which constitutes the eastern segment of the northern margin of the North China Craton. The rock types of the Saima Deposit include phonolite, nepheline syenite, and aegirine nepheline syenite, which hosts niobium–tantalum ore bodies. In this study, the primary niobium-bearing minerals identified include loparite, betafite, and fersmite. The Saima pluton is characterized as a potassium-rich, low-sodium, and peraluminous alkaline pluton. Trace element characteristics reveal that the metallization-associated syenite is enriched in large-ion lithophile elements (LILEs) such as K and Rb but is relatively depleted in high-field strength elements (HFSEs). As indicated by the rare earth element (REE) profile, the Saima pluton exhibits a high total REE content (Σ REE), dominance of light REEs (LREEs), and scarcity of heavy REEs (HREEs). The Sr-Nd-Pd isotopic data suggest that aegirine nepheline syenite and nepheline syenite share consistent isotopic signatures, indicating a common origin. The Saima alkaline pluton displays elevated I_{Sr} values ranging from 0.70712 to 0.70832 coupled with low $\epsilon_{Nd}(t)$ values between -12.84 and -11.86 and two-stage model ages (t_{DM2}) from 1967 to 2047 Ma. These findings indicate that the metallogenic materials for the Saima Deposit derive from both an enriched mantle source and some crustal components. The lithium (Li) isotopic fractionation observed during the genesis of the Saima pluton could be attributed to the differential diffusion rates of 6Li and 7Li under non-equilibrium fluid–rock interactions.

Keywords: eastern Liaoning province; Saima alkaline rock-hosted niobium–tantalum deposit; niobium–tantalum minerals; Sr-Nd-Pb isotopes; Li isotopes



Citation: Wu, Y.; Ju, N.; Liu, X.; Shi, L.; Feng, Y.; Ma, D. Sources of Metallogenic Materials of the Saima Alkaline Rock-Hosted Niobium–Tantalum Deposit in the Liaoning Region: Evidence from the Sr-Nd-Pb and Li Isotopes. *Minerals* **2023**, *13*, 1443. <https://doi.org/10.3390/min13111443>

Academic Editor: Pierre Schiano

Received: 26 September 2023
Revised: 29 October 2023
Accepted: 13 November 2023
Published: 15 November 2023



Copyright: © 2023 by the authors. Licensee MDPI, Basel, Switzerland. This article is an open access article distributed under the terms and conditions of the Creative Commons Attribution (CC BY) license (<https://creativecommons.org/licenses/by/4.0/>).

1. Introduction

Alkaline rocks account for about 1% of the total magmatic rocks on earth. They are known for their complex mineral composition, containing more than 50% of the total minerals discovered so far [1]. Alkaline rock is rich in large-ion lithophile elements, rare earth and high field strength elements. It is a heavy ore body containing REE, Zr, Nb and Ta, which has a huge economic value [2]. For example, the Kvanefjeld uranium polymetallic deposit related to the lujarite complex in southern Greenland not only contains tens of thousands of tons of uranium oxide (U_3O_8) but also millions of tons of rare earth oxides (TREO). It is also associated with a large number of Nb, Ta and other rare metals [3]. The Thor Lake rare earth polymetallic deposit related to the aegirine nepheline syenite complex in Canada contains a large amount of strategic metal resources such as zirconium, niobium, and heavy rare earth (HREE) [4].

China's alkaline rocks, which occupy a limited outcrop area, are scattered across Xinjiang, the Panxi Rift Valley, Qinba, and the Liaodong Peninsula. The alkaline pluton in the Saima area of Liaoning province stands out due to its pronounced differentiation

and evolution, complex lithologies, alkali pegmatite exposures, rich mineral diversity, and a plethora of rare metal resources, including U, Th, Zr, Nb, and REEs. Consequently, the Saima pluton serves as an exemplary case for examining the petrology, mineralogy, genesis, magmatic evolution, and rare metal enrichment and mineralization mechanisms associated with alkaline rocks and their rare metal–rare earth element deposits. The Saima alkaline complex is mainly composed of potassic magmatites such as early hornblende syenite and aegirine nepheline syenite, and late soditic lujarite with high magmatic evolution and obvious magmatic hydrothermal activity traces. It provides a unique research window for exploring the geochemical behavior of uranium, thorium and rare earth elements during the evolution of alkaline magma [5–7]. Based on a detailed study of the chemical composition of the rinkite, Wu [8] found that not only is the rinkite continuously enriched, but also the contents of high-field strength elements such as Nb, Zr and REE (especially HREE) are continuously increased from nepheline syenite through aegirine nepheline syenite pegmatite to late lujarite.

Integrating the previous studies on the Saima alkaline pluton, the genesis of the niobium–tantalum deposit is not clear, and there is no direct lithological evidence of the niobium–tantalum mineral. Strengthening and deepening the relevant research can reveal the formation mechanism of alkaline rocks and related deposits and have certain enlightenment for guiding regional prospecting. Based on the characteristics of Sr–Nd–Pb isotope and Li isotope, the source of metallogenic materials and the metallogenic mechanism of the niobium–tantalum element in the Saima niobium–tantalum deposit are studied systematically by petrography and mineralogy.

2. Regional Geological Setting

The Saima deposit is located to the south of the Taizihe–Hunjiang paleodepression and to the north of the Yingkou–Kuandian uplift (Figure 1) [5,9]. It forms a segment of the Saima alkaline pluton within the northeastern part of the North China Craton. The E–W trending Saima pluton spans an outcrop area of approximately 200 km², with the primary ore-controlling structure oriented to the northeast. Overlying strata in this region encompass the Lower Proterozoic Gaxian and Dashiqiao formations, the Upper Proterozoic Xihe Group, the Paleozoic Cambrian and Ordovician strata, and the Mesozoic Jurassic strata. These strata present complex lithologies, transitioning from nepheline syenite in the initial phase to lujavrite in the subsequent phase. The Saima pluton's main petrogenic minerals comprise potassium feldspar, nepheline, biotite, aegirite, and eudialyte. Distinctive accessory minerals within the pluton include zircon, potassium zircon, stratosilica–cerium titanite, and eudialyte. The nepheline syenite comprises the main body (70%) of the pluton [5]. The aegirine syenite rich in green, grass green and taupe aegirine has better mineralization, while the mineralization degree of pegmatite formed in late evolution is higher. The boundary between nepheline syenite and aegirine nepheline syenite is transitional, indicating that their formation was contemporaneous. Multiple alteration types, such as those involving microplagioclase, nepheline, sodium zeolite, and gannetite, as well as carbonation, are evident in the Saima pluton. Its niobium–tantalum mineralization is closely associated with aegirine nepheline syenite [10]. The primary magma of the Saima alkaline rock was initially rich in niobium [11]. The eastern Liaoning area is positioned within the Liaodong rift tectonic belt, and the Mesozoic rift reactivation transpired during the Indosinian intracontinental fault orogeny amidst a backdrop of crustal thickening.

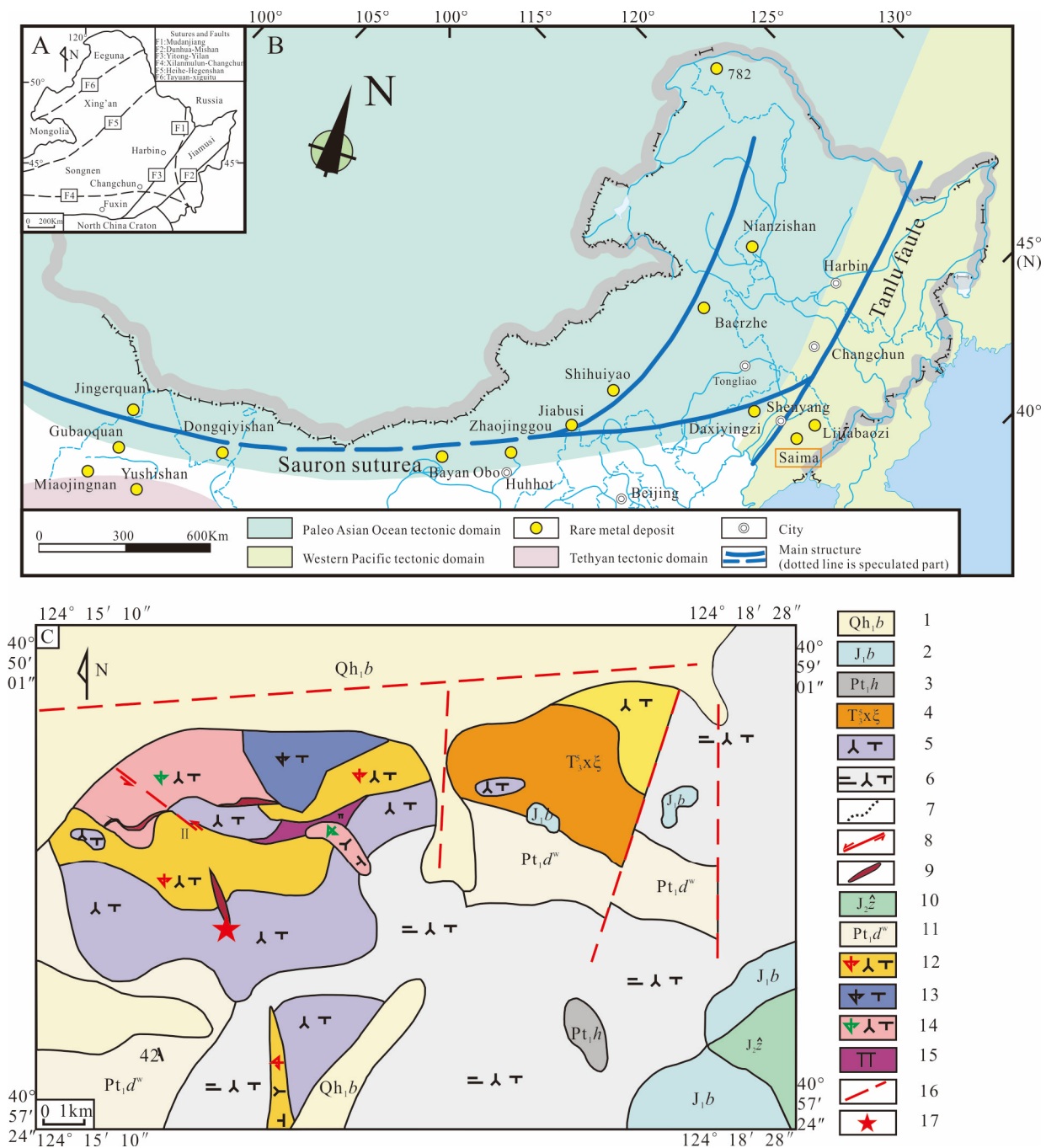


Figure 1. Geotectonic location map. (A) Geological sketch map (modified from reference [9]). (B) Distribution map of rare earth deposits in northeast China (Modified from reference [9]). (C) Geological map of the Saima deposit (Modified from reference [5]). 1. Quaternary alluvium; 2. Jurassic Beimiao formation; 3. Huaziyu formation of Liaohe group; 4. Late Triassic Saima diamicctite; 5. Late Triassic nepheline syenite; 6. Late Triassic biotite–nepheline syenite; 7. Angular unconformity; 8. parallel displacement fault; 9. Nb ore body and number; 10. Jurassic Zhuanshanzi formation; 11. Wangjiagou rockbody of the Liaohe group; 12. Late-Triassic brown ijolite syenite; 13. Late Triassic aegirine syenite; 14. Late Triassic grass—green aegirine ijolite syenite; 15. Late Triassic intrusive rock (nepheline phonolite); 16. Supposed fault; 17. Sample location.

The Saima alkaline pluton exhibits complex lithologies, with its ages determined using a range of methods. The U-Pb ages of eudialyte from nepheline syenite, obtained through laser ablation inductively coupled plasma mass spectrometry (LA-ICP-MS), were

224 ± 4 Ma [12]. The zircon U-Pb ages from aegirine nepheline syenite, as determined via LA-ICP-MS, were 231.9 ± 3.7 Ma and 229.5 ± 2.2 Ma [9,10] and 230–224 Ma using SIMS [13]. The ^{40}Ar - ^{39}Ar ages for biotite from altered nepheline syenite and nepheline syenite pegmatite were 234.3 ± 6.3 Ma and 230.08 ± 2.75 Ma, respectively [11]. The Saima Deposit experienced mineralization during the Late Triassic within the Late Indosinian post-collisional continental rifting or extensional setting. Wu [14,15] found two new minerals from the Saima alkaline complex, fluorsigaiite- $\text{Ca}_2\text{S}_3(\text{PO}_4)_3\text{F}$ and gysinite-(La), $\text{PbLa}(\text{CO}_3)_2(\text{OH})\cdot\text{H}_2\text{O}$.

Prior experimental studies have categorized the petrogenetic models of alkaline rocks into two primary types. The first suggests that alkaline rocks derive from the continual crystallization differentiation of alkaline basaltic magma, potentially with crustal assimilation [16,17]. The second posits that these rocks arise from the partial melting of metasomatized ultramafic rocks within the subcontinental lithospheric mantle, enriched in large-ion lithophile and light rare earth elements (LILEs and LREEs) [18–20]. Zhu [13] proposed that both silica-saturated and silica-undersaturated rocks in the Saima area shared a similar age and originated from low-degree partial melting of a mantle source rich in clinopyroxene lithosphere with contributions from carbonatite and amphibolite within the garnet stability field. Approximately 60% of the continental components were implicated in the source of the Saima alkaline rocks. Ju [9] argued that the niobium-rich aegirine nepheline syenite was a product of crust-mantle interaction and crystallized within a post-collisional continental rift setting. Fu [21] concluded that alkaline magmatic evolution is controlled by fluid-unsaturated pure magmatic systems, while hyperalkaline magmatic rocks are formed in a fluid-supersaturated magmatic system.

3. Analytical Methods

3.1. Mineral Compositions

Six pristine aegirine nepheline syenite samples enriched in niobium and tantalum minerals were chosen, pulverized, and polished into thin sections for backscatter image observation and EPMA. Backscattered electron images of these minerals were acquired, and a qualitative assessment of their compositions was conducted using a JOEL JAX-IT500 scanning electron microscope at the MLR Key Laboratory of Metallogeny and Mineral Assessment, Chinese Academy of Geological Sciences. The quantitative compositional analysis was performed using a JOEL JXA-8100 electron probe at the laboratory of the Shenyang Center, China Geological Survey. Operating parameters for the electron probe were an accelerating voltage of 15 kV, a beam current of 20 nA, and a beam diameter of 2 μm. Distinctive spectral lines of various elements were differentiated using four spectroscopic crystals: LIF, TAP, PETH, and PETJ. Standard samples employed to calibrate REE measurements were synthetic rare-earth phosphates, while standards for elements like Ti, Si, Nb, and Ta comprised rutile, microcline, niobium, tantalum, and scheelite. For major elements such as Si, Al, Mg, Ca, Fe, Na, and K, the measurement and background measurement times for their characteristic peaks were 10 s and 5 s, respectively. For trace elements, including P, Nb, Ti, Zr, Cr, Y, Mn, Sr, Ba, and REEs, these times were 20 s and 10 s, respectively. All data underwent ZAF correction, achieving an accuracy better than ±0.5 wt%.

3.2. Major- and Trace-Element Geochemistry

Eleven rock samples were collected from the surface exploratory trenches and the surrounding rocks of the TCG-11 ore body within the Saima Deposit. Samples SMK-1 through SMK-6 were aegirine nepheline syenite exhibiting grass-green exteriors, whereas samples SMW-1 through SMW-5 were characterized as light flesh-red nepheline syenites. Petrographic examinations of these samples were conducted at the laboratory of the Shenyang Center, China Geological Survey, with mineral structures and compositions ascertained using an Olympus BX51 polarized light microscope.

Primarily sourced from the surface exploratory trenches of the Saima Deposit, these samples showed negligible mineralization and alteration. They were subsequently crushed and ground using an agate mill. Comprehensive analyses for major and trace elements, as well as REEs, were undertaken at the Shenyang Center laboratory, employing an ARL-PERFORM'X wavelength dispersive XRF for the first two and an ICP-MS analyzer for REEs. A total of 50 mg of powdered sample was dissolved in 0.01 mL of HClO₄. A combination of 1.5 mL of HF and 1.5 mL of HNO₃ was sealed in a Teflon bomb and heated on a 140 °C plate until dry. Following this, the dried mixture was sealed and incubated within a steel jacket in an oven at 195 °C for 48 h. Post-evaporation, 3 mL of HNO₃ was added and heated until dried. An additional 3 mL of HNO₃ was then introduced, and the new mixture was sealed and reheated in an oven at 140 °C for 12 h. Upon cooling, the resultant solution was decanted and diluted to a 100 g volume. One gram of rhodium was integrated into the diluted solution as an internal standard, facilitating the tracking of potential drifts during mass spectrometric evaluations. Analytical precisions for the major and trace elements predominantly surpassed 5% and 10%, respectively.

3.3. Sr-Nd-Pb Isotopic Analyses

The Sr-Nd-Pb isotopic analyses were conducted using a Neptune Plus MC-ICP-MS, produced by Thermo Fisher Scientific (Waltham, MA, USA), at Beijing Createch Testing Technology Co., Ltd. (Beijing, China). A 120 mg sample of whole-rock powder was digested in a steel-jacketed Teflon bomb with 2.5 mL of HF, 0.2 mL of HNO₃, and HClO₄. The bomb was then placed in an oven at 195 °C for one week. Post-dissolution, the mixture was dried with fuming HClO₄ on a hot plate. Subsequently, 6 mL of HCl was added and evaporated to complete dryness. To transform fluorides into chlorides, an additional 6 mL of HCl was introduced. The isotopic ratios of Sr, Nd, and Pb were corrected using exponential normalization with values of $^{88}\text{Sr}/^{86}\text{Sr} = 8.375209$, $^{146}\text{Nd}/^{144}\text{Nd} = 0.7219$, and $^{203}\text{Tl}/^{205}\text{Tl} = 0.418922$, respectively. The detailed laboratory protocols for Sr, Nd, and Pb isotopic determinations and analyses can be found in Yang [22,23].

3.4. Li Isotopes in Whole Rocks and Minerals

Li isotope testing in minerals was conducted at Nanjing FocuMS Technology Co., Ltd. Detailed procedures for Li isotope analysis are outlined in the referenced literature [24–26]. Initially, a 30–40 mg sample of 200-mesh powder was placed in a PFA open dissolution bottle, followed by the addition of HNO₃ and HF in a 1:5 ratio, ensuring thorough mixing by shaking. The dissolution bottle underwent ultrasonic oscillation for 10 min and was then placed on a heating plate at 100–120 °C for 24 h until granulated residues formed. Afterward, the bottle was uncapped and heated until complete acid evaporation. Post-dryness, HNO₃ was added 2–4 times, and the bottle was reheated at 100–120 °C for another 24 h. Lastly, 1 mL of concentrated HCl was added and heated for 24 h until dried.

Li isotopes were analyzed using the Nu Plasma II multi-collector MC-ICP-MS from the UK's Nu Instruments Ltd. and the ASI RESolution LR 193 nm ArF excimer laser from Australian Scientific Instruments. The internal precision, external precision, and accuracy surpassed 0.005%, 0.05%, and 0.05%, respectively. Both the ⁶Li and ⁷Li isotopes were simultaneously measured using the low-mass and high-mass Faraday cups (i.e., L4 and H4, respectively). For the Li isotopes, plasma sources produced notable isotopic discrimination, particularly for ions with relatively low atomic masses (about 25% of Li isotope mass fractionation). However, these effects can be accurately corrected using standard samples [27]. The test sequence was blank sample 1 → standard sample 1 → blank sample 2 → sample 1 → blank sample 3 → standard sample 2 → blank sample 4 → sample 2.

4. Analytical Results

4.1. Petrographic Characteristics

4.1.1. Aegirine Nepheline Syenite

The petrographic analysis reveals that the aegirine nepheline syenite comprises aegirine (30%), nepheline (15%), and potassium feldspar (55%). The grass-green aegirine displays pronounced pleochroism, presenting as euhedral to subhedral elongated, needle-like crystals with grain sizes ranging from 0.4–3.6 mm. The nepheline, which occupies the interstices and spaces between potassium feldspar grains, exhibits grain sizes of 0.3–2.2 mm. The grain size of the potassium feldspar varies from 1.6–4.0 mm (Figure 2).

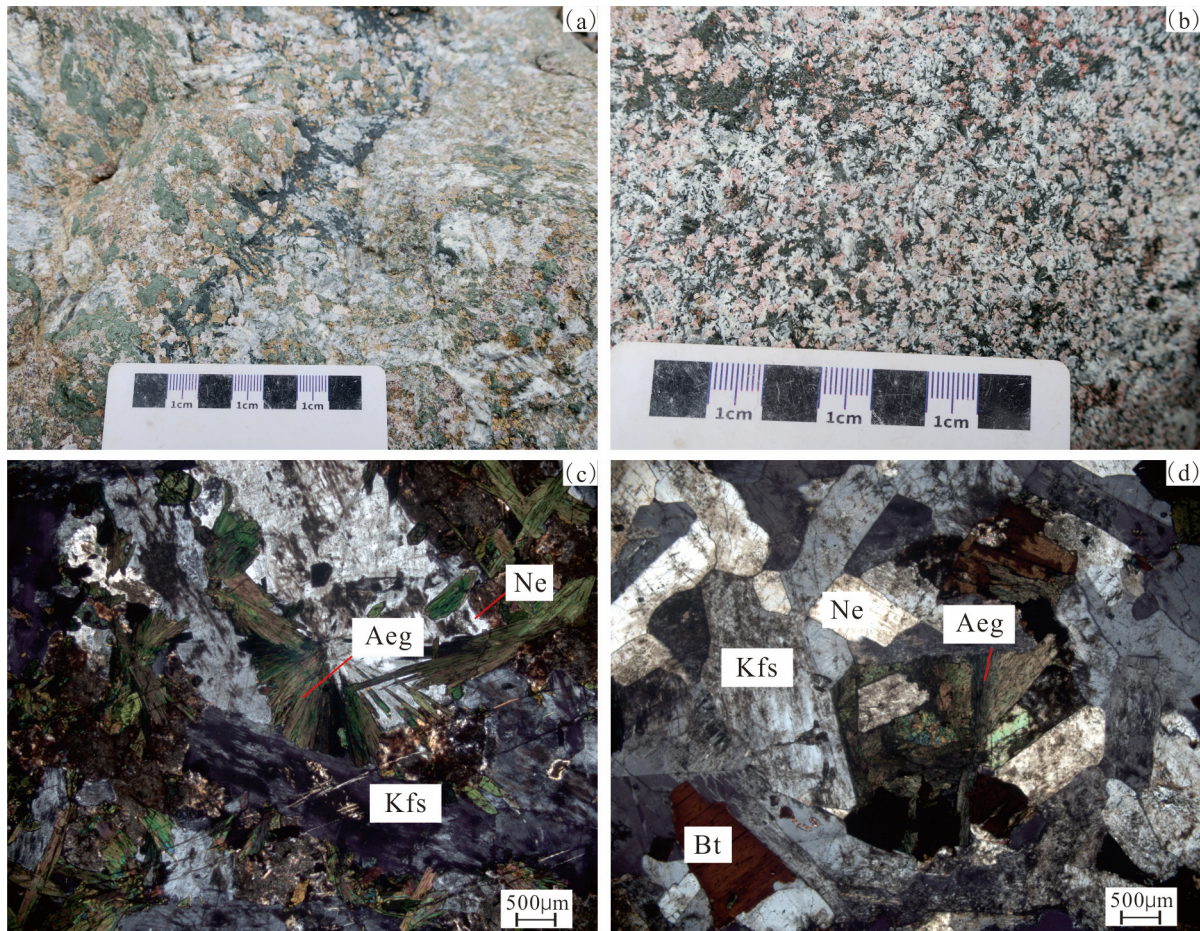


Figure 2. Field and photomicrographs of the Saima deposit. (a) Coarse medium-grained biotite nepheline syenite. (b) Aegirine nepheline syenite. (c) Aegirine nepheline syenite. (d) Biotite nepheline syenite.

4.1.2. Nepheline Syenite

The coarse- to medium-grained biotite nepheline syenite is composed of potassium feldspar, biotite, and nepheline. These minerals exhibit grain sizes between 2.6–10 mm, with nepheline occurring at the margins and interstices of the potassium feldspar grains.

4.2. Mineralogical Features

Based on EPMA results for mineral composition, the primary minerals identified are loparite, fersmite, and betafite. Owing to the substitution of many REEs by isomorphism, the rare earth oxides can have two types of cations, termed group A and group B, which exhibit subtle differences. Detailed analysis of mineral occurrence and variations in chemical composition across different lithologies can shed light on the geochemical behaviors and metallogenic processes of REEs during the evolution of alkaline magma. Quantitative EPMA results are provided in Table 1.

Table 1. EPMA-derived compositions of representative niobium-bearing minerals in nepheline syenite (wt%).

Sample	SMK-1-1	SMK-1-2	SMK-6-1	SMK-6-2	SMK-2-1	SMK-2-2	SMK-4-1	SMK-4-2	SMK-3-1	SMK-3-2	SMW-4-1	SMW-4-2
Minerals	Loparite				Betafite				Fersmite			
Al ₂ O ₃	0.98	1.67	1.64	2.11	0.36	0.33	1.46	0.57	1.34	0.61	0.10	0.16
SiO ₂	2.55	3.94	4.21	3.98	5.13	3.27	6.02	5.43	3.65	2.87	2.05	2.34
TiO ₂	34.69	33.78	34.60	35.39	16.28	13.84	13.06	12.73	7.86	7.60	7.61	8.78
CaO	0.94	0.87	1.88	1.87	2.12	2.65	12.46	10.79	12.15	14.62	14.46	14.72
K ₂ O	0.94	0.79	1.31	1.74	4.33	1.51	—	—	0.54	0.62	1.39	1.59
Nb ₂ O ₅	8.70	8.59	6.59	6.23	50.36	53.72	32.80	34.68	51.55	52.64	56.83	53.54
Y ₂ O ₃	7.81	9.94	10.29	9.79	—	—	—	—	0.79	0.83	—	—
Ce ₂ O ₃	21.84	20.61	18.92	18.94	—	—	5.73	5.92	2.44	2.54	2.65	2.73
MnO	2.04	3.92	—	—	—	—	—	—	—	—	—	—
La ₂ O ₃	13.98	10.60	9.32	8.77	—	—	—	—	2.35	2.77	1.43	1.73
Pr ₂ O ₃	3.74	3.68	—	—	—	—	—	—	—	—	—	—
PbO	—	—	3.80	3.66	6.08	8.89	1.90	2.16	—	—	1.21	1.25
ThO ₂	—	—	1.78	1.59	—	—	—	—	—	—	—	—
ZrO ₂	—	—	3.55	3.53	—	—	—	—	2.07	1.91	3.57	4.01
UO ₂	—	—	—	—	12.64	13.99	18.67	18.83	8.19	7.56	3.59	3.74
Na ₂ O	—	—	—	—	0.96	-	—	—	—	—	—	—
SrO	—	—	—	—	—	—	3.92	5.58	3.13	2.72	2.96	3.29
MgO	—	—	—	—	—	—	0.12	-	—	—	—	—
Ta ₂ O ₅	—	—	—	—	—	—	1.14	0.86	—	—	0.62	0.52
ThO ₂	—	—	—	—	—	—	—	—	0.44	0.98	—	—
BaO	—	—	—	—	—	—	—	—	4.05	1.89	—	—
Total	98.21	98.40	97.9	97.6	98.25	98.19	96.14	96.69	99.76	99.33	98.49	98.40
Calculated in units of 2 oxygen atoms												
Al	0.03	0.06	0.06	0.07	0.02	0.02	0.10	0.04	0.09	0.04	0.01	0.01
Si	0.08	0.12	0.13	0.12	0.29	0.19	0.34	0.31	0.21	0.16	0.12	0.13
Ti	0.78	0.76	0.78	0.80	0.70	0.59	0.56	0.54	0.34	0.33	0.33	0.38
Ca	0.03	0.03	0.12	0.06	0.13	0.16	0.76	0.66	0.74	0.89	0.88	0.90
K	0.04	0.03	0.05	0.07	0.31	0.11	—	—	0.04	0.05	0.10	0.12
Nb	0.12	0.12	0.09	0.08	1.29	1.38	0.84	0.89	1.33	1.36	1.46	1.38
Y	0.12	0.16	0.16	0.16	—	—	—	—	0.02	0.03	—	—
Ce	0.24	0.23	0.21	0.21	0.00	—	0.12	0.12	0.05	0.05	0.06	0.06
Mn	0.05	0.10	—	—	—	—	—	—	—	—	—	—
La	0.15	0.12	0.10	0.10	—	—	—	—	0.05	0.06	0.03	0.04
Pr	0.04	0.04	—	—	—	—	—	—	—	—	—	—
Pb	—	—	0.03	0.03	0.09	0.14	0.03	0.03	—	—	0.02	0.02
Th	—	—	0.01	0.01	—	—	—	—	—	—	—	—
Zr	—	—	0.05	0.05	—	—	—	—	0.06	0.05	0.10	0.11
U	—	—	—	—	0.16	0.18	0.24	0.24	0.10	0.19	0.05	0.05
Na	—	—	—	—	0.11	—	—	—	—	—	—	—
Sr	—	—	—	—	—	—	0.13	0.18	0.10	0.09	0.10	0.11
Mg	—	—	—	—	—	—	0.01	-	—	—	—	—
Ta	—	—	—	—	—	—	0.02	0.01	—	—	0.01	0.01
Th	—	—	—	—	—	—	—	—	0.01	0.01	—	—
Ba	—	—	—	—	—	—	—	—	0.09	0.04	—	—

A. Fersmite

Fersmite, a pneumatolytic-hydrothermal mineral, can replace pyrochlore and be substituted by niobite with a determined chemical formula of CaNb₂O₆. In sample SMK-3, fersmite appeared as xenomorphic granular formations within fractures (Figure 3a,b), with particle sizes between approximately 10–30 µm. In sample SMW-4, fersmite was found in potassium feldspar fissures due to metasomatic events, exhibiting an automorphic-hypidiomorphic texture and particle sizes from 15–80 µm. The backscattered electron images indicated that larger fersmite particles displayed high automorphic characteristics

and rhythmic zonings of varying brightness, centered by zircon. Fersmite in both aegirine nepheline syenite and biotite nepheline syenite primarily consisted of CaO (12.148–14.622 wt%), TiO₂ (7.604–8.777 wt%), and Nb₂O₅ (51.552–56.827 wt%), with consistent primary chemical components and minor REE variations.

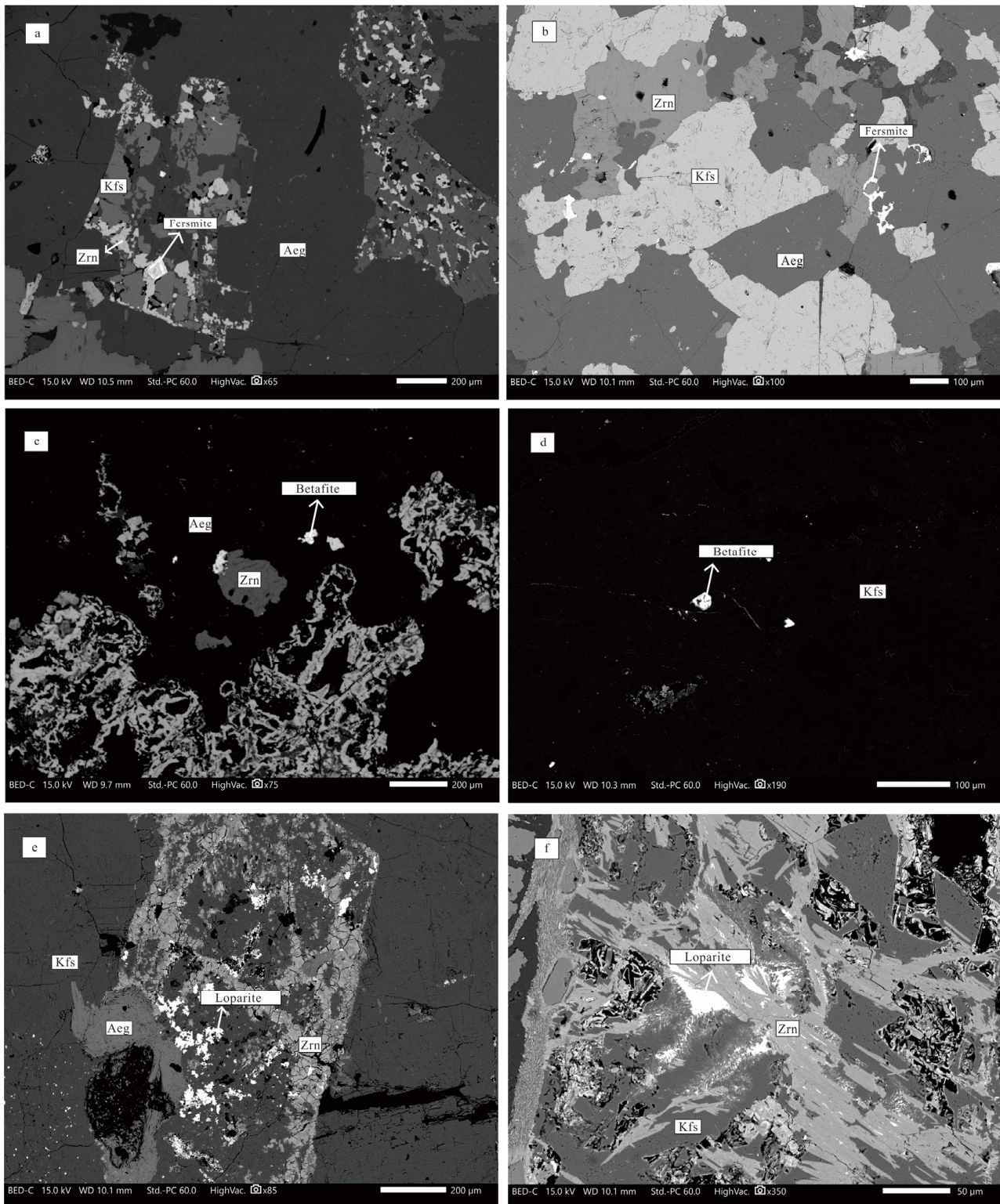


Figure 3. Backscatter images of niobium-bearing minerals. (a,b) Fersmite; (c,d) Betafite; (e,f) Loparite.

B. Betafite

The deduced chemical formula for betafite is $(Ca,U)_2(Ti,Nb,Ta)_2O_6(OH)$. With its high titanium and uranium contents, betafite can be differentiated from pyrochlore. It presented an automorphic-hypidiomorphic granular texture in the Saima Deposit, sporadically distributed on potassium feldspar surfaces (SMK-2, SMK-4; Figure 3c,d) and coexisting with zircon. The particle size ranged widely from about 5–50 μm , suggesting ample space for automorphic growth. The backscattered electron images showed that betafite grains had consistent surfaces without any compositional zoning due to localized alterations and different chemical compositions. The betafite in the aegirine nepheline syenite primarily consisted of TiO_2 (12.726–16.283 wt%), Nb_2O_5 (32.682–53.716 wt%), and UO_2 (12.636–18.833 wt%), indicating largely consistent primary chemical elements with minor REE variations.

C. Loparite

The chemical formula of loparite, $(Ce,Na,Ca)(Ti,Nb)O_3$, was determined based on mineral composition analysis. Loparite in the Schryburt Lake carbonate complex, north-west of Lake Ontario, Canada, continuous interaction with fluorine-rich fluids resulted in a local environment rich in Ti, Na, Nb, and rare earths [28]. Loparite was found only sporadically in some aegirine nepheline syenite samples. Under the optical microscope, it exhibited a xenomorphic granular texture, with particle sizes between approximately 15–35 μm . Most loparite in the samples localized on the surface of altered potassium feldspar, near zircon (SMK-1), and within pores or reticular fissures on feldspar surfaces resulting from metasomatism (SMK-6). Interactions between hydrothermal fluids and surrounding rocks induced chemical changes and replacements, leading to new mineral formations in vacant spaces. Thus, loparite formed during later metasomatism. Backscattered electron images indicated that loparite grains had consistent surfaces devoid of compositional zoning caused by localized alterations and different chemical compositions (Figure 3e,f). As detailed in Table 1, the loparite in aegirine nepheline syenite primarily comprised TiO_2 (33.783–35.394 wt%), Nb_2O_5 (6.234–8.698 wt%), Ce_2O_3 (18.92–21.842 wt%), Y_2O_5 (7.813–10.29 wt%), and La_2O_3 (8.77–13.978 wt%), showing largely uniform primary chemical constituents with minor REE variations.

Within niobium-rich alkaline rocks, the primary diagenetic mineral was potassium feldspar. Transitioning from rare-earth-rich to niobium–tantalum-rich alkaline rocks, titanium-bearing minerals progressively decreased, with rock textures evolving from coarse-grained to intermediate and fine-grained structures.

4.3. Lithochemical Characteristics

4.3.1. Major Elements

The major elemental composition of aegirine nepheline syenite from the Saima Deposit is presented in Table 2, revealing specific characteristics. Six aegirine nepheline syenite samples displayed SiO_2 , TiO_2 , P_2O_5 , and Al_2O_3 contents ranging from 46.8–54.0 wt%, 0.68–1.37 wt%, 0.016–0.035 wt%, and 16.9–21.2 wt%, respectively. The ore-forming pluton was characterized by elevated total alkali contents ($K_2O + Na_2O$) between 12.00%–17.04%, high potassium ratios ($K_2O/Na_2O = 1.41$ – 3.90), and Rittmann indices ($\sigma = [\omega(K_2O + Na_2O)]^2 / [\omega(SiO_2 - 43)]$) ranging from 26.47–37.92, indicative of alkaline rocks. All six samples were positioned within the nepheline syenite zone on the total alkali-silica (TAS) diagram (Figure 4a), classifying them within the alkaline rock series. Additionally, they predominantly resided in the peraluminous rock zone in the A/NK-A/CNK discrimination plot (Figure 4b) and the alkaline granite zone in the $w(K_2O)$ - $w(SiO_2)$ rock series discrimination plot (Figure 4c).

Table 2. Contents of major elements (wt%) and trace elements (ppm) of the aegirine nepheline syenite and nepheline syenite in the Saima Deposit.

Sample	SMK-1	SMK-2	SMK-3	SMK-4	SMK-5	SMK-6	SMW-1	SMW-2	SMW-3	SMW-4	SMW-5
Rock Name	Aegirine nepheline syenite						Nepheline syenite				
SiO ₂	51.1	51.5	49.7	53.3	54.0	46.8	53.6	51.7	54.6	54.5	53.2
Al ₂ O ₃	15.2	15.9	16.9	21.2	20.3	20.4	19.4	20.3	7.34	20.6	21.1
TFe ₂ O ₃	12.6	11.6	8.62	4.24	4.74	13.0	7.46	8.38	20.9	4.09	4.71
MgO	0.44	0.20	2.05	0.28	0.60	0.05	0.05	0.03	0.04	0.37	0.01
CaO	1.03	1.00	2.59	0.55	0.61	0.05	0.74	0.94	0.14	0.36	1.24
Na ₂ O	10.0	9.82	2.98	4.41	3.74	4.97	6.21	6.02	9.77	3.63	5.66
K ₂ O	5.98	6.49	11.6	12.2	13.3	7.03	9.02	8.83	4.89	12.8	11.1
MnO	0.46	0.43	0.29	0.23	0.22	0.45	0.23	0.24	0.45	0.23	0.17
TiO ₂	1.37	1.31	3.49	0.68	0.75	1.43	0.24	0.24	1.12	0.54	1.10
P ₂ O ₅	0.02	0.02	0.45	0.04	0.11	0.01	0.01	0.03	0.01	0.05	0.01
LOI	1.72	1.67	1.62	2.84	1.46	5.56	3.00	3.12	0.70	2.80	1.51
Ba	458	484	2187	1918	3661	246	664	750	197	2017	970
Cr	27.2	32.2	21.0	31.3	26.3	21.7	21.3	29.5	21.0	26.4	28.3
Li	124	82.3	133	54.6	51.0	83.0	52.0	274	11.8	56.1	7.60
Be	21.6	18.6	6.18	15.8	8.88	29.2	25.8	18.4	12.0	11.4	8.58
Sc	9.65	9.09	5.65	1.07	2.89	7.74	3.12	2.67	2.29	2.29	3.96
Co	7.25	11.2	21.9	6.29	9.31	3.93	4.37	3.66	5.66	5.90	3.38
Ni	4.18	2.36	5.64	2.21	2.49	6.01	1.91	1.54	5.30	2.47	2.50
Ga	50.6	50.9	22.5	24.6	20.5	57.0	39.2	47.6	66.8	19.6	23.3
Rb	152	131	460	517	453	240	255	241	204	585	296
Sr	6412	6939	2971	2759	2283	621	716	758	145	2269	1275
Zr	11,900	11,600	722	1400	413	8500	874	953	2800	962	588
Nb	340	375	94.5	65.3	37.8	244	16.3	18.9	53.1	42.0	51.5
Hf	86.0	214	20.7	29.2	8.40	161	24.1	27.7	73.8	21.1	16.4
Ta	19.6	18.3	11.3	4.31	2.99	11.3	5.56	4.47	2.14	2.83	3.88
Pb	1800	2000	72.0	140	42.8	840	68.7	288	47.9	58.4	68.7
Th	55.0	51.4	21.3	12.9	31.2	36.7	21.9	28.9	30.9	13.7	11.3
U	25.3	21.2	5.97	16.7	12.7	20.5	5.75	7.58	5.39	5.80	2.25
La	206	213	273	169	141	226	21.2	48.8	30.7	105	77.1
Ce	419	425	665	268	298	610	38.8	89.4	63.0	180	193
Pr	43.7	46.0	71.3	22.4	29.6	52.7	3.84	8.83	7.08	17.3	24.5
Nd	170	174	310	76.0	102	213	12.3	24.1	25.8	50.9	83.8
Sm	43.5	41.0	46.2	9.30	13.8	45.6	1.90	3.84	4.59	6.88	12.9
Eu	13.2	12.6	11.8	2.81	4.63	11.4	0.59	1.18	1.17	2.33	3.43
Gd	41.4	39.6	31.3	7.42	11.0	37.0	1.47	3.26	3.78	5.50	8.57
Tb	8.19	7.68	3.73	0.83	1.33	5.82	0.22	0.39	0.60	0.66	1.07
Dy	48.8	45.3	13.9	3.15	5.61	29.1	0.96	1.57	3.35	2.77	4.05
Ho	9.24	8.77	1.89	0.52	0.93	4.75	0.18	0.26	0.70	0.48	0.60
Er	28.2	26.9	4.86	1.45	2.65	13.2	0.53	0.74	2.28	1.30	1.46
Tm	4.91	4.62	0.55	0.22	0.40	2.10	0.11	0.13	0.42	0.19	0.20
Yb	31.2	29.4	2.85	1.42	2.45	13.2	0.86	1.09	2.66	1.15	1.26
Lu	4.22	3.98	0.30	0.21	0.32	1.69	0.16	0.21	0.35	0.16	0.20

The major elemental composition of nepheline syenite from the Saima Deposit revealed distinct characteristics. Five biotite nepheline syenite samples displayed SiO₂, TiO₂, P₂O₅, and Al₂O₃ contents of 51.7%–54.6%, 0.24%–1.12%, 0.0079%–0.050%, and 19.4%–21.1%, respectively, highlighting pronounced metaluminous properties. The surrounding rocks exhibited elevated total alkali contents (K₂O + Na₂O) in the range of 14.66%–16.79%, high potassium ratios (K₂O/Na₂O = 1.45–3.53), and Rittmann indices ($\sigma = [\omega(K_2O + Na_2O)]^2 / [\omega(SiO_2 - 43)]$) primarily between 18.54–27.60, confirming the alkaline nature of these samples. All five samples were positioned within the nepheline syenite zone on the TAS diagram (Figure 4a), categorizing them within the alkaline rock series. Additionally, they were located in the peraluminous rock zone in the A/NK-A/CNK discrimination plot

(Figure 4b) and the alkaline granite zone in the $w(\text{K}_2\text{O})$ - $w(\text{SiO}_2)$ rock series discrimination plot (Figure 4c).

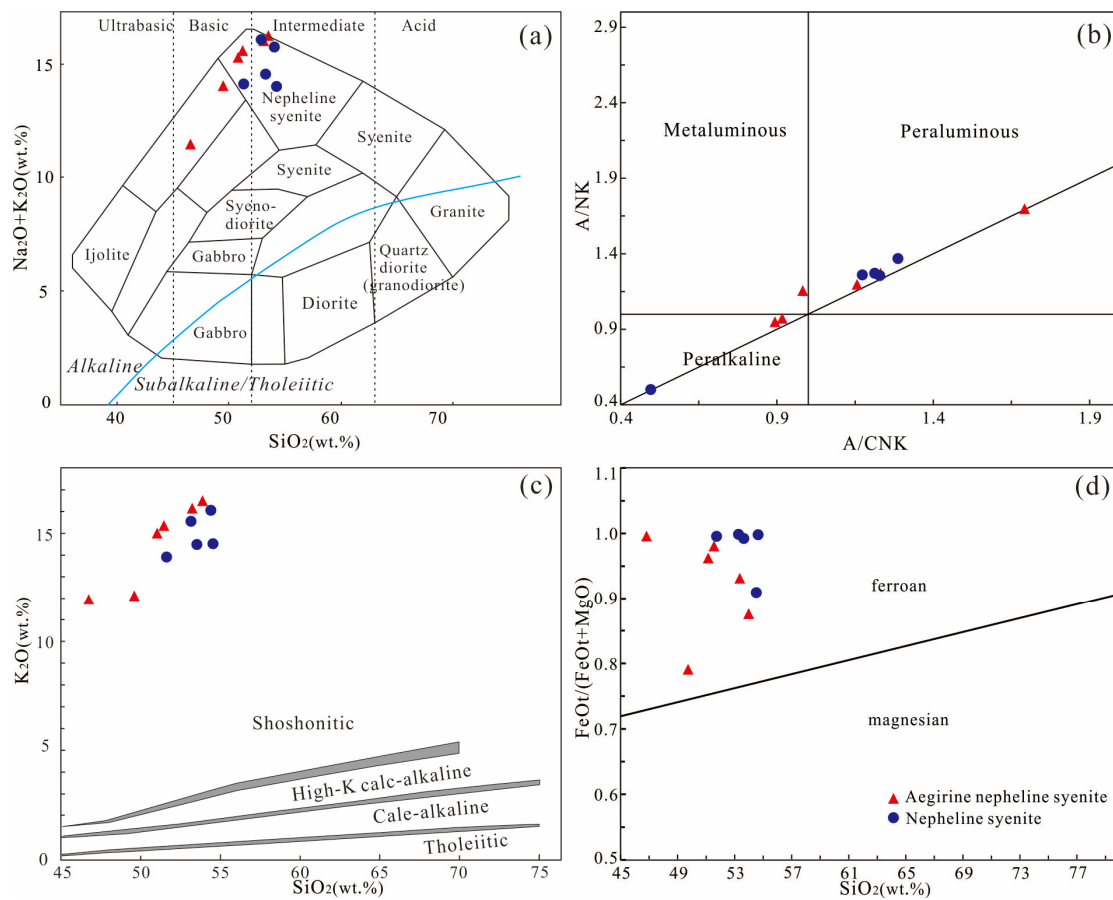


Figure 4. Geochemical diagrams showing the major elements of aegirine nepheline syenite and nepheline syenite in the Saima Deposit. (a) TAS diagram (after [29]). (b) A/NK-A/CNK diagram (after [30]). (c) K_2O - SiO_2 diagram (after [31]). (d) $\text{FeOt}/(\text{FeOt} + \text{MgO})$ - SiO_2 diagram of ore-forming plutons of the Saima and Baerzhe deposits (after [32]).

4.3.2. Trace Elements

The REE analytical data (Table 2) indicate that the Saima Deposit possesses exceptionally high $\sum\text{REE}$ values and pronounced REE fractionation. The aegirine nepheline syenite and nepheline syenite samples from the Saima Deposit exhibited $\sum\text{REE}$ values primarily in the range of 563.06×10^{-6} – 1436.56×10^{-6} and 83.00×10^{-6} – 373.77×10^{-6} , respectively. Consequently, the $\sum\text{REE}$ values for the aegirine nepheline syenite samples were roughly fivefold compared to those of the nepheline syenite samples. Furthermore, the individual REE contents in the ore-forming pluton exceeded those in the adjacent rocks by up to a factor of ten.

The aegirine nepheline syenite samples from the Saima Deposit had LREE (such as La, Ce, Pr, Nd, Sm, and Eu) contents ranging from 547.84×10^{-6} – 1377.11×10^{-6} and heavy rare earth element (HREE, such as Gd, Tb, Dy, Ho, Er, Tm, Yb, and Lu) contents ranging from 15.21×10^{-6} – 176.16×10^{-6} . Hence, their LREE/HREE ratios were between 5.08–36.01, averaging 17.42. REE analyses (Figure 5) indicate that the syenite from the Saima Deposit displays pronounced LREE enrichment and HREE depletion, with LaN/YbN ratios spanning 4.74–85.44, averaging $36.27 > 10$ [33–35], and distinctly rightward REE distribution curves, signifying notable LREE and HREE fractionation. The ore-forming pluton did not display significant Sr and Eu anomalies ($\delta\text{Eu} = 2\text{EuN}/(\text{SmN} + \text{GdN})$; 0.85–1.15). The nepheline syenite samples from the Saima Deposit had LREE and HREE contents ranging

from 78.52×10^{-6} – 394.39×10^{-6} and 4.48×10^{-6} – 17.39×10^{-6} , respectively. Therefore, their LREE/HREE ratios were from 9.36–29.62, averaging 20.44. The nepheline syenite samples had LaN/YbN ratios ranging from 8.28–65.34 and $\delta\text{Eu} = 2\text{EuN}/(\text{SmN} + \text{GdN})$ values between 0.86–1.16 [36,37].

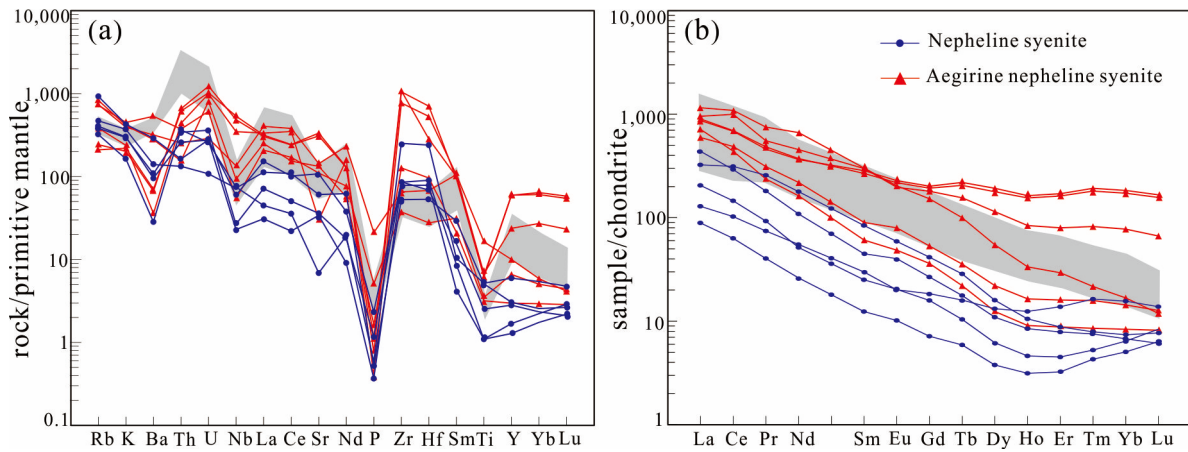


Figure 5. Primitive mantle-normalized trace element spider diagrams (a) and chondrite-normalized REE patterns (b) of the aegirine nepheline syenite and nepheline syenite in the Saima deposit [38]. The grey field is the data from Ju [9].

4.4. Sr-Nd-Pb Isotopes

The aegirine nepheline syenite and nepheline syenite samples from the Saima deposit displayed consistent Sr-Nd isotopic characteristics (Table 3). They had $^{87}\text{Sr}/^{86}\text{Sr}$ and $^{143}\text{Nd}/^{144}\text{Nd}$ ratios ranging from 0.708528843–0.710648378 and 0.511816536–0.511941865, respectively. Based on the rock age of 224 Ma [9], their I_{Sr} , $\epsilon_{\text{Nd}}(t)$, $f_{\text{Sm}/\text{Nd}}$, and t_{DM} values calculated were 0.70712–0.70832, -12.84 – -11.86 , -0.61 – -0.18 , and 1967–2047 Ma, respectively. The high I_{Sr} values and low $\epsilon_{\text{Nd}}(t)$ values imply that the source rocks originated primarily from the crustal materials.

Table 3. Sr-Nd-Pb isotopic compositions of the Saima deposit.

Sample	SMK-1	SMK-3	SMK-4	SMK-5	SMK-6	SMW-1	SMW-2	SMW-4
Rock Name	Aegirine nepheline syenite					Nepheline syenite		
t(Ma)	224	224	224	224	224	224	224	224
$^{87}\text{Rb}/^{86}\text{Sr}$	0.066751	0.437760	0.529536	0.560739	1.090988	1.005113	0.899047	0.728126
$^{87}\text{Sr}/^{86}\text{Sr}$	0.708529	0.709622	0.709802	0.709842	0.710648	0.710324	0.710058	0.710271
$^{147}\text{Sm}/^{144}\text{Nd}$	0.160598	0.093791	0.076910	0.084378	0.134784	0.097483	0.100186	0.084921
$^{143}\text{Nd}/^{144}\text{Nd}$	0.511942	0.511846	0.511821	0.511839	0.511912	0.511884	0.511850	0.511817
I_{Sr}	0.70832	0.70823	0.70812	0.70806	0.70717	0.70712	0.70719	0.70795
$\epsilon_{\text{Sr}}(t)$	58	56.7	55.1	54.3	41.7	40.9	41.9	52.7
$f_{\text{Rb}/\text{Sr}}$	-0.19	4.29	5.4	5.78	12.19	11.15	9.87	7.8
I_{Nd}	0.511706	0.511709	0.511708	0.511715	0.511715	0.511742	0.511703	0.511692
$t_{\text{DM}2}$	2012	2019	2021	2010	2005	1967	2027	2047
$\epsilon_{\text{Nd}}(t)$	-12.56	-12.5	-12.52	-12.39	-12.39	-11.86	-12.62	-12.84
$f_{\text{Sm}/\text{Nd}}$	-0.18	-0.52	-0.61	-0.57	-0.31	-0.5	-0.49	-0.57
$^{206}\text{Pb}/^{204}\text{Pb}$	16.945133	17.059080	17.112741	17.246771	17.018350	17.983013	16.994215	17.100560
$^{207}\text{Pb}/^{204}\text{Pb}$	15.505977	15.514526	15.517586	15.523648	15.515068	15.540079	15.508530	15.516513
$^{208}\text{Pb}/^{204}\text{Pb}$	36.996076	37.155187	37.053145	37.489011	7.034726	37.859821	37.068329	37.160730
$(^{206}\text{Pb}/^{204}\text{Pb})_i$	16.915	16.88	16.857	16.603	16.966	17.798	16.937	16.886
$(^{207}\text{Pb}/^{204}\text{Pb})_i$	15.504	15.505	15.505	15.491	15.512	15.531	15.506	15.506
$(^{208}\text{Pb}/^{204}\text{Pb})_i$	36.975	36.947	36.989	36.972	37.004	37.63	36.998	36.995

These samples from the Saima deposit demonstrated consistent Pb isotopic characteristics (Table 3). They had $^{206}\text{Pb}/^{204}\text{Pb}$, $^{207}\text{Pb}/^{204}\text{Pb}$, and $^{208}\text{Pb}/^{204}\text{Pb}$ ratios ranging from 16.945133–17.983013, 15.505977–15.540079, and 36.996076–37.859821, respectively. Their initial $(^{206}\text{Pb}/^{204}\text{Pb})_i$, $(^{207}\text{Pb}/^{204}\text{Pb})_i$, and $(^{208}\text{Pb}/^{204}\text{Pb})_i$ ratios calculated were 16.603–17.798, 15.491–15.531, and 36.947–37.63, respectively.

4.5. Whole-Rock and Mineral Li Isotopic Compositions

The Li contents and isotopic compositions of the whole rocks and specific minerals from the Saima alkaline pluton are detailed in Table 4. The nepheline syenite sample from the Saima region had Li content of 39.0 ppm, notably lower than the 94.3 ppm observed in the aegirine nepheline syenite sample. Conversely, the $\delta^7\text{Li}$ value of the nepheline syenite sample (2.2‰) exceeded the 2.04‰ of the aegirine nepheline syenite sample. Ore-forming minerals such as mica, potassium feldspar, and aegirine in the aegirine nepheline syenite displayed varied Li contents and isotopic compositions. The nepheline's Li isotopic composition was not measured due to its exceedingly low Li content (0.37 ppm). Potassium feldspar exhibited Li content of 17.9 ppm and a notably low Li isotopic composition, with a $\delta^7\text{Li}$ value of -22.44% . Aegirine presented Li content of 27.3 ppm and a $\delta^7\text{Li}$ value of -0.35% . Contrasting with potassium feldspar and aegirine, mica registered a remarkably high Li content of 542 ppm and a $\delta^7\text{Li}$ value of 1.49‰. Beyond the Li isotopes of aegirine, the Li isotopes in syenite, aegirine nepheline syenite, mica, and potassium feldspar all aligned with the mid-oceanic ridge basalt (MORB) range.

Table 4. Li isotopic compositions of the Saima alkaline pluton.

Rock/mineral	Sample	Li	$\delta^7\text{Li}$	2SD	
Nepheline syenite	SM-21-32	39.0	2.2	0.07	
Aegirine nepheline syenite	SM-21-28	94.3	2.04	0.27	
Mica in aegirine nepheline syenite	SM-21-28-1	542	1.49	0.25	
Nepheline in aegirine nepheline syenite	SM-21-28-2	0.375			
Feldspar in aegirine nepheline syenite	SM-21-28-3	17.9	-22.44	0.19	
Aegirine in aegirine nepheline syenite	SM-21-28-4	27.3	-0.35	0.14	
REE(ppm)	Nb	Ta	Zr	Hf	Li
SM-21-28	37.8	2.99	413	8.4	39
SM-21-32	16.3	5.56	874	24.1	94.3
SM-21-28-2	18.9	4.47	953	27.7	542
SM-21-28-1	53.1	2.14	2800	73.8	0.375
SM-21-28-3	42	2.83	962	21.1	17.9
SM-21-28-4	51.5	3.88	588	16.4	27.3

5. Discussion

5.1. Material Sources

The genesis of syenite remains debated. Prior comprehensive research has identified three potential origins: crust-derived magma, mantle-derived magma, and a combination of both crust- and mantle-derived magma [33,39]. Spidergrams of primitive mantle-normalized trace elements present rightward curves, suggesting the syenite from the Saima deposit is LILE-rich and HFSE-depleted, pointing towards a mantle-derived origin [40]. These spidergrams also illustrate that Ba has conspicuous troughs when contrasted with Rb and Th, aligning with continental crust rock traits outlined by Zhou [41]. The trace element partitioning in the aegirine nepheline syenite resembles the shadow patterns in REE data presented by Ju [9], underscoring a shared source. In addition, the syenite from the Saima deposit exhibited Rb/Sr ratios between 0.16–1.41, surpassing the continental crust's value of 0.15 [42,43]. Such features advocate for the blending of magmatic sources with crustal constituents. Collectively, the REE and trace element profiles of the syenite from the Saima align with the stance of Zhao [44] regarding the combined crust- and mantle-derived magma. Thus, the magmatic genesis of the Saima pluton can be attributed

to mantle sources intermixed substantially with crustal components during its ascent or emplacement.

Typically, magma inherits the isotopic composition of its progenitor rocks, achieving isotopic equilibrium at high temperatures. This equilibrium persists even when a later-formed closed system undergoes differentiation. Hence, examining igneous rocks offers insights into the isotopic signatures of the deep earth. Furthermore, Sr-Nd-Pb isotopes are potent tracers for delineating rock material origins. The syenite from the Saima deposit exhibited elevated I_{Sr} values between 0.70712–0.70832, reduced $\epsilon_{Nd}(t)$ values from -12.84 – -11.86 , and t_{DM2} values spanning 1967–2047 Ma, suggesting a source predominantly influenced by crust-derived materials. All samples positioned themselves within the crust-mantle transition zone (B-C zone; Figure 6a) in the I_{Sr} - $\epsilon_{Nd}(t)$ plot, indicating a commingling of the magma with mantle-derived constituents. Furthermore, the $^{207}Pb/^{204}Pb$ - $^{206}Pb/^{204}Pb$ and $^{208}Pb/^{204}Pb$ - $^{206}Pb/^{204}Pb$ plots (Figure 6b,c) reveal that all samples align closely with the lower crust and enriched mantle I domains and Pb isotope sources were influenced by enriched mantle I end-members, inferring interactions between mantle-derived magma and crustal materials [45]. Yan [46] and Ren [47] posited that the material sources of Mesozoic Indosinian alkali-rich intrusive rocks in the North China Craton correlate with an enriched mantle (akin to enriched mantle I) amalgamated with crustal components. The derived conclusions indicate that the material sources of the aegirine nepheline syenite and nepheline syenite align with the regional sources of the Saima deposit [48].

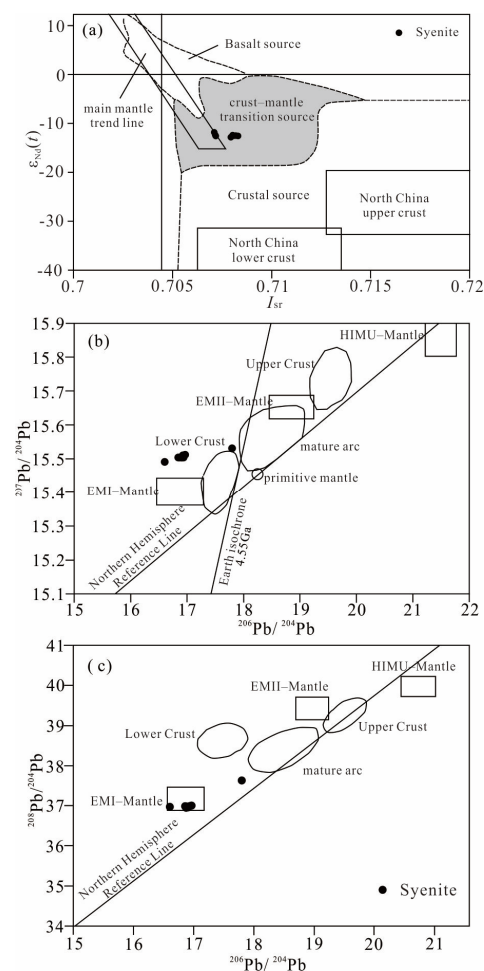


Figure 6. Magmatic source area diagrams of ore-forming rock plutons in the Saima (a) modified from [49]; (b,c) modified from [50]) (EMI, EMII, HIMU and Primitive Mantle after [51]; lower crust, mature arc and upper crust after Zartman et al. [50]).

5.2. Li Isotopic Characteristics of the Saima Alkaline Pluton and Their Implications

The rare-metal alkaline rocks of Saima have experienced pronounced magmatic differentiation, which is pivotal for the diversity of their mineralization [4,52]. Consequently, comprehending magmatic differentiation is essential to further elucidate the enrichment of rare metal elements and the ultimate mineralization processes within rare-metal alkaline rocks. Li plays an indispensable role as a volatile element during magmatic differentiation, and the accumulation patterns of Nb and, notably, Ta [53] vary within the magmatic differentiation of rare-metal alkaline rocks [54]. The Li isotopic composition can act as a potent geochemical tracer for this differentiation. The nepheline syenite and aegirine nepheline syenite at Saima exhibited markedly diverse Li isotopic compositions. Likewise, the mica, potassium feldspar, and aegirine in the aegirine nepheline syenite displayed varied Li isotopic profiles, suggesting Li isotope fractionation during the Saima pluton's genesis. Typically, the mechanisms triggering Li isotope fractionation correlate with magmatic evolutionary stages, encompassing crystallization differentiation and fluid dynamics, which include water-rock interactions and ion diffusion in fluids.

5.2.1. Li Isotope Fractionation during the Magmatic Differentiation

Magmatic differentiation impacts whole-rock Li isotopes predominantly through fractional crystallization and Li isotopic shifts within certain lithium-rich minerals, principally mica, followed by feldspar, quartz, pyroxene, and amphibole. Mica serves as the primary Li-bearing mineral in alkaline rocks due to its Li partition coefficient being substantially higher than those of other minerals, such as feldspar and aegirine. Experimental evidence indicates that Li exhibits slight compatibility in biotite ($D_{\text{Li biotite/melt}} = 0.8\text{--}1.67$; [55]) and is moderately incompatible in feldspar ($D_{\text{Li feldspar/melt}} = 0.1\text{--}0.68$; [55]). Consequently, pronounced crystallization differentiation of these minerals, especially biotite, can influence the Li content in silicate melts. The Li isotope fractionation is governed by Li's coordination within mineral structures and the solid/melt partition coefficients [56]. ^7Li is preferentially incorporated into lower coordination phases, while ^6Li is more favored in higher coordination phases [57]. Typically, Li occupies the octahedral coordination site in most diagenetic minerals (e.g., pyroxene, amphibole, feldspar, and mica [58]). In contrast, tetrahedral coordination is predominant in silicate melts. Thus, if mica is the main fractionating mineral during differentiation, the remaining melts will exhibit a relatively heavy Li isotopic composition.

Crystal-melt fractionation is a pivotal mechanism for the genesis of pegmatite melts. While the aegirine nepheline syenite and nepheline syenite share analogous mineral assemblages, the aegirine nepheline syenite, characterized by extremely elevated alkali content (such as Li and Cs) and diminished rare earth content, cannot form solely from equilibrium crystallization of conventional nepheline syenite melts. Maneta [59] posited that spodumene in lithium-cesium-tantalum (LCT) pegmatite could crystallize from a Li-supersaturated residual melt enriched in H_2O and fluxing agents (e.g., F, B, and P). Such a residual melt might undergo upwards of 80% crystallization differentiation, incorporating minerals like feldspar and quartz [60]. Yet, this is not observed in the Saima deposit's aegirine nepheline syenite, which is more differentiated than nepheline syenite and exhibits higher Nb/Ta ratios (Figure 7a). Within the Saima pluton, the Li content in aegirine nepheline syenite markedly surpasses that in nepheline syenite. Furthermore, mica in aegirine nepheline syenite has anomalously elevated Li content compared to the surrounding matrix. Mica exhibits the most pronounced Li content in aegirine nepheline syenite, succeeded by aegirine, potassium feldspar, and nepheline. Therefore, the remarkable Li enrichment in aegirine nepheline syenite reflects its advanced differentiation and is consistent with the elevated Li content in mica. However, the nepheline syenite and aegirine nepheline syenite display subtle disparities in their whole-rock $\delta^7\text{Li}$ values (Figure 7b), ranging between 2.20‰ and 2.04‰. This implies that unless mica serves as the primary fractionating mineral, magmatic differentiation does not induce pronounced Li isotope fractionation. The $\delta^7\text{Li}$ values of the two rock types exhibit an inverse relationship

with magmatic differentiation: the more evolved aegirine nepheline syenite possesses lower $\delta^7\text{Li}$ values than its less evolved counterpart, the nepheline syenite. The Li isotopic variations in the Saima deposit cannot be rationalized by mere crystal-melt fractionation, as the differentiation of diagenetic minerals should lead to a heavier Li isotopic composition in the residual melt. The divergence between whole-rock Li isotope fractionation and magmatic differentiation might stem from potent fluid–rock interactions.

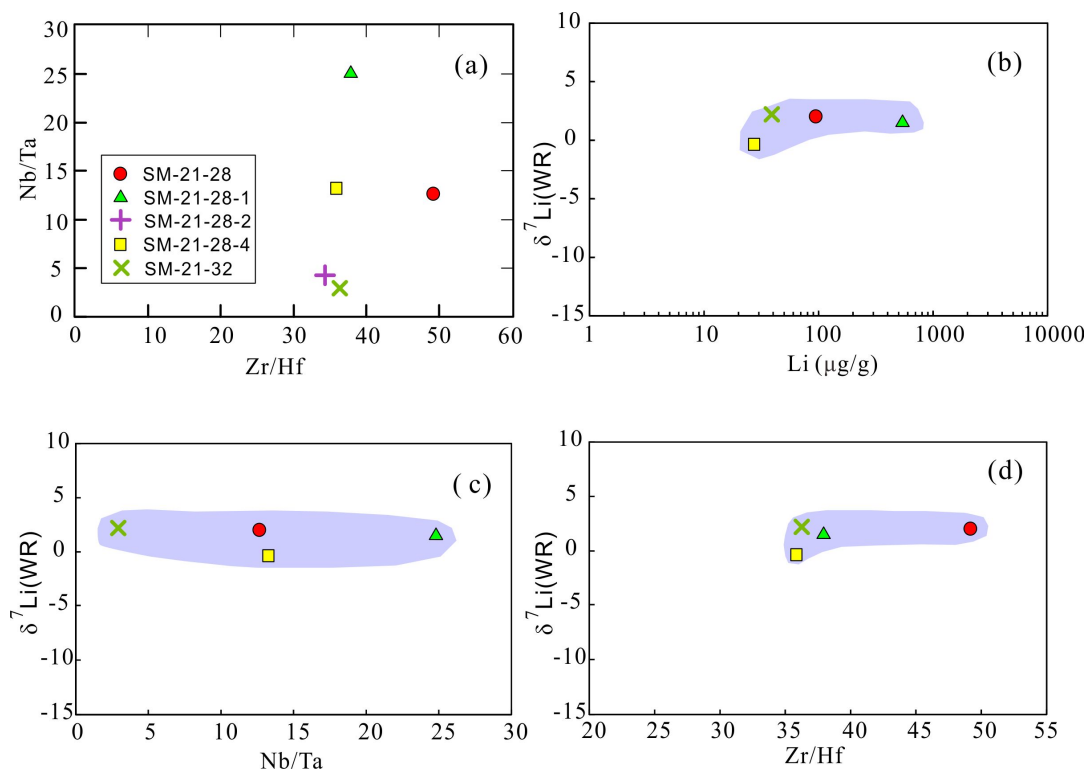


Figure 7. Plots of Li isotope fractionation: Nb/Ta-Zr/Hf (a), whole-rock $\delta^7\text{Li}$ versus Li content (b), whole-rock $\delta^7\text{Li}$ -Nb/Ta (c), and whole-rock $\delta^7\text{Li}$ -Zr/Hf plots (d).

5.2.2. Diffusion-Driven Li Isotope Fractionation

The aegirine nepheline syenite sample from the Saima pluton exhibited a notably lower $\delta^7\text{Li}$ value of 2.04‰ compared to the nepheline syenite sample (2.20‰). This discrepancy may predominantly arise from mica crystallization. However, this is incongruent with the observed upward trend in Li content within mica during differentiation. Certain biotite samples from the Saima pluton, marked by indistinct boundaries, were metasomatized by natrolite and hydromuscovite, hinting at a restricted fluid–rock interaction. Consequently, Li isotope fractionation between the mica and fluid phases does not seem to elucidate the $\delta^7\text{Li}$ values observed in samples from the Saima pluton.

Given the considerable mass disparity between Li isotopes, ^6Li diffuses approximately 3% more rapidly than ^7Li in melts, fluids, minerals, and rocks. Diffusion experiments have shown that mica can experience swift and significant alterations in its Li isotopic composition due to interactions with Li-rich fluids. Moreover, mica generally possesses higher $\delta^7\text{Li}$ values than its adjacent fluids, as ^6Li transitions from mica to fluids more efficiently than ^7Li . This phenomenon suggests that the preferential diffusion of lighter ^6Li isotopes from mica into fluids results in elevated $\delta^7\text{Li}$ values within rocks. Li displays rapid diffusion in minerals. Minerals within the Saima pluton’s aegirine nepheline syenite exhibit non-equilibrium Li partitioning (Figure 7), with marked disparities in Li contents (542, 17.9, and 27.3, respectively) and isotopes ($\delta^7\text{Li}$ values: 1.49, −22.44, and −0.35, respectively) between mica, potassium feldspar, and nepheline. Consequently, the differential diffusion

velocities of Li isotopes during non-equilibrium fluid–rock interactions contribute to the Li isotope fractionation observed in the Saima pluton.

5.2.3. Indications for the Mineralization of Rare Metals

The mineralization of niobium, zirconium, and rare earth elements is intricately tied to magmatic differentiation, and achieving saturation of rare metals and Li-bearing minerals in alkaline melts demands substantial magmatic fractionation [61]. Various magmatic processes can give rise to distinct metallogenic mechanisms in rare-metal alkaline rocks [62]. The Saima alkaline pluton stands as a representative rare-metal deposit, featuring mineralization of rare earth elements, zirconium, and niobium, while showcasing pronounced Li isotopic variations. The Saima pluton presents marked differences in Li contents and Nb/Ta and Zr/Hf ratios; however, the $\delta^7\text{Li}$ values in the nepheline syenite and aegirine nepheline syenite samples show only modest reductions. This suggests that extensive magmatic differentiation may result in only minor Li isotope fractionation. The Li isotope fractionation within the Saima pluton might arise from fluid–rock interactions. Nevertheless, petrographic observations indicate that only a subset of biotite exhibits blurred boundaries, undergoing replacement by natrolite and hydromuscovite. This observation infers that the volume of fluid exsolution was insufficient to trigger significant lithium isotope fractionation, and Li leaching had a negligible impact on the Li isotope fractionation in nepheline syenite and aegirine nepheline syenite samples. The diffusion rate of ^6Li surpasses that of ^7Li by 3%. Notable variances in the Li contents and isotopic shifts among minerals in the aegirine nepheline syenite sample might stem from the differential diffusion rates of the two Li isotopes.

Hence, the Li isotope fractionation in samples from the Saima pluton might be ascribed to fluid diffusion. In summary, the Li isotope fractionation in the Saima pluton can be traced back to diverse magmatic differentiation processes, which play a pivotal role in the unique mineralization of rare earth elements, zirconium, and niobium in rare-metal alkaline rocks.

6. Conclusions

- (1) The Saima deposit, located within potassium-rich, low-sodium peraluminous alkaline rocks, is dominated by aegirine nepheline syenite and nepheline syenite. The electron probe results show that the main niobium-bearing minerals in the Saima deposit are loparite, betafite, and fersmite, which are mainly found in the aegirine nepheline syenite, while only fersmite is identified within the biotite nepheline syenite. Additionally, as one transitions from REE-rich to niobium–tantalum-rich alkaline rocks, the presence of titanium-bearing minerals diminishes, and the texture shifts from coarse-grained to intermediate and fine-grained structures.
- (2) All samples display a pronounced, indicative of LREE enrichment and HREE depletion. Such patterns suggest that deep hydrothermal fluids from both the crust and mantle contributed to the crystallization of these samples. Both the aegirine nepheline syenite and nepheline syenite in the Saima Deposit exhibit consistent Sr–Nd–Pd isotopic characteristics, encompassing elevated I_{Sr} values, negative $\epsilon_{Nd}(t)$ values, and two-stage model ages spanning 1967–2047 Ma. From these data, it can be deduced that the material sources of the Saima Deposit are tied to an enriched mantle with some degree of crustal material mixing. The material sources of the aegirine nepheline syenite and nepheline syenite align with the broader regional sources of the Saima Deposit.
- (3) The Li isotope fractionation observed during the Saima pluton's formation can likely be attributed to the faster diffusion rate of ^6Li compared to ^7Li during non-equilibrium fluid–rock interactions. Distinct magmatic differentiation impacts on Li isotope fractionation emerge as a crucial mechanism, driving the varied mineralization of rare earth elements, zirconium, and niobium in rare-metal alkaline rocks.

Author Contributions: Methodology, Y.W.; Writing-original draft, Y.W.; Investigation, N.J.; Funding acquisition, N.J.; Data curation, X.L.; Formal analysis, L.S.; Visualization, Y.F.; Supervision, Y.F.; Resources, D.M. All authors have read and agreed to the published version of the manuscript.

Funding: This research was funded by National Natural Science Foundation of China, grant number [42102087], China Postdoctoral Science Foundation, grant number [2022M712966], National Natural Science Foundation of China, grant number [U2244201], Major project of the Ministry of Science and Technology, grant number [2021QZKK0304]. And The APC was funded by [42102087].

Data Availability Statement: The authors confirm that the data generated or analyzed during this study are provided in full within the published article.

Acknowledgments: The authors thank Li Xiaowei from the China University of Geosciences for the help with the data processing, as well as the reviewers for their valuable comments.

Conflicts of Interest: The authors declare no conflict of interest. Yue Wu has received research grants from the foundation [42102087].

References

1. Yang, Z.; Giester, G.; Ding, K.; Tillmanns, E. Hezuolinite, $(\text{Sr, REE})_4\text{Zr}(\text{Ti, Fe}^{3+}, \text{Fe}^{2+})_2\text{Ti}_2\text{O}_8(\text{Si}_2\text{O}_7)_2$, a new mineral species of the chevkinite group from Saima alkaline complex, Liaoning Province, NE China. *Eur. J. Mineral.* **2012**, *24*, 189–196. [\[CrossRef\]](#)
2. Wooley, A.R. *Alkaline Rocks and Carbonatites of the World. Part3: Africa*; The Geological Society Publishing House: London, UK, 2001.
3. Greenland Minerals and Energy LTD. Greenland Minerals 2021 AGM Presentation. Available online: <http://wcsecure.welink.com.au/pdf/GGG/02504612.pdf> (accessed on 20 March 2022).
4. Sheard, E.R.; Williams-Jones, A.E.; Heiligmann, M.; Pederson, C.; Trueman, D.L. Controls on the concentration of zirconium, niobium, and the rare earth elements in the Thor Lake rare metal deposit, Northwest Territories, Canada. *Econ. Geol.* **2012**, *107*, 81–104. [\[CrossRef\]](#)
5. Chen, Z.B.; Fan, J.; Guo, Z.T.; He, Z.Q.; Wang, S.L.; Ren, K.C. *Saima Alkaline Rocks and Metallogenesis*; Atomic Energy Press: Beijing, China, 1996; pp. 1–19. (In Chinese with English abstract)
6. Liu, Y.; Zhu, Z.; Chen, C.; Zhang, S.; Sun, X.; Yang, Z.; Liang, W. Geochemical and mineralogical characteristics of weathered ore in the Dalucao REE deposit, Mianning–Dechang REE Belt, western Sichuan Province, southwestern China. *Ore Geol. Rev.* **2015**, *71*, 437–456. [\[CrossRef\]](#)
7. Wu, B.; Wang, R.C.; Yang, J.H.; Wu, F.Y.; Zhang, W.L.; Gu, X.P.; Zhang, A.C. Zr and REE mineralization in sodic lujauvrite from the Saima alkaline complex, northeastern China: A mineralogical study and comparison with potassic rocks. *Lithos* **2016**, *262*, 232–246. [\[CrossRef\]](#)
8. Wu, B.; Wang, R.C.; Guo, G.L.; Song, Z.T. Compositional variations of rinkite in the Saima alkaline complex, Liaoning Province, and its implications for alkaline magma evolution. *Earth Sci.* **2020**, *45*, 467–478. (In Chinese with English abstract)
9. Ju, N.; Ren, Y.-S.; Zhang, S.; Bi, Z.-W.; Shi, L.; Zhang, D.; Shang, Q.-Q.; Yang, Q.; Wang, Z.-G.; Gu, Y.-C.; et al. Metallogenic Epoch and Tectonic Setting of Saima Niobium Deposit in Fengcheng, Liaoning Province, NE China. *Minerals* **2019**, *9*, 80. [\[CrossRef\]](#)
10. Cheng, X.; Xu, J.; Zhang, H.; He, B. U-Pb Geochronology and Geochemistry of Zircon from the Saima-Bailinchuan Alkaline Intrusion in Eastern Liaoning, China. *Acta Geol. Sin. Engl. Ed.* **2014**, *88*, 959–962. [\[CrossRef\]](#)
11. Ma, D.Z.; Liu, Y. Nb mineralization in the nepheline syenite in the Saima area of the North China Craton, China. *Ore Geol. Rev.* **2023**, *152*, 105247. [\[CrossRef\]](#)
12. Wu, F.Y.; Yang, Y.H.; Marks, M.A.; Liu, Z.C.; Zhou, Q.; Ge, W.C.; Yang, J.S.; Zhao, Z.F.; Mitchell, R.H.; Markl, G. In situ U–Pb, Sr, Nd and Hf isotopic analysis of eudialyte by LA-(MC)-ICP-MS. *Chem. Geol.* **2010**, *273*, 8–34. [\[CrossRef\]](#)
13. Zhu, Y.S.; Yang, J.H.; Sun, J.F.; Zhang, J.H.; Wu, F.Y. Petrogenesis of coeval silica-saturated and silica-undersaturated alkaline rocks: Mineralogical and geochemical evidence from the Saima alkaline complex, NE China. *J. Asian Earth Sci.* **2016**, *117*, 184–207. [\[CrossRef\]](#)
14. Wu, B.; Gu, X.P.; Rao, C.; Wang, R.C.; Xing, X.Q.; Zhong, F.J.; Wan, J.J.; Bonnetti, C. Fluorsigaiite, $\text{Ca}_2\text{S}_3(\text{PO}_4)_3\text{F}$, a new mineral of the apatite supergroup from the Saima alkaline complex, Liaoning Province, China. *Mineral. Mag.* **2022**, *86*, 940–947. [\[CrossRef\]](#)
15. Wu, B.; Gu, X.P.; Rao, C.; Wang, R.C.; Xing, X.Q.; Wan, J.J.; Bonnetti, C. Gysinite-(La), $\text{PbLa}(\text{CO}_3)_2(\text{OH})\cdot\text{H}_2\text{O}$, a new rare earth mineral of the ancylite group from the Saima alkaline complex, Liaoning Province, China. *Mineral. Mag.* **2023**, *87*, 143–150. [\[CrossRef\]](#)
16. Zhang, Z.; Qin, J.; Lai, S.; Long, X.; Ju, Y.; Wang, X.; Zhu, Y. Origin of Late Permian amphibole syenite from the Panxi area, SW China: High degree fractional crystallization of basaltic magma in the inner zone of the Emeishan mantle plume. *Int. Geol. Rev.* **2020**, *62*, 210–224. [\[CrossRef\]](#)
17. Abdel-Karim, A.A.; Azer, M.; Sami, M. Petrogenesis and tectonic implications of the Maladob ring complex in the South Eastern Desert, Egypt: New insights from mineral chemistry and whole-rock geochemistry. *Int. J. Earth Sci.* **2021**, *110*, 53–80. [\[CrossRef\]](#)

18. Yang, H.; Lai, S.C.; Qin, J.F.; Zhu, R.Z.; Zhao, S.W.; Zhu, Y.; Zhang, F.Y.; Zhang, Z.Z.; Wang, X.Y. Early Palaeozoic alkaline trachytes in the North Daba Mountains, South Qinling Belt: Petrogenesis and geological implications. *Int. Geol. Rev.* **2021**, *63*, 2037–2056. [[CrossRef](#)]
19. Choi, E.; Fiorentini, M.L.; Giuliani, A.; Foley, S.F.; Maas, R.; Graham, S. Petrogenesis of Proterozoic alkaline ultramafic rocks in the Yilgarn Craton, Western Australia. *Gondwana Res.* **2021**, *93*, 197–217. [[CrossRef](#)]
20. Moghadam, H.S.; Hoernle, K.; Hauff, F.; Garbe-Schönberg, D.; Pfänder, J. Geochemistry and petrogenesis of alkaline rear-arc magmatism in NW Iran. *Lithos* **2022**, *412*, 106590. [[CrossRef](#)]
21. Fu, R.X.; Li, N.B.; Niu, H.C.; Shan, Q.; Zhao, X.; Liu, K. Magmatic evolution and rare earth element enrichment of Saima alkaline complex, Liaoning, China. *Acta Petrol. Sin.* **2023**, *39*, 2951–2967. (In Chinese with English abstract) [[CrossRef](#)]
22. Yang, Y.H.; Zhang, H.F.; Chu, Z.Y.; Xie, L.W.; Wu, F.Y. Combined chemical separation of Lu, Hf, Rb, Sr, Sm and Nd from a single rock digest and precise and accurate isotope determinations of Lu-Hf, Rb-Sr and Sm-Nd isotope systems using Multi-Collector ICP-MS and TIMS. *Int. J. Mass Spectrom.* **2010**, *290*, 120–126. [[CrossRef](#)]
23. Yang, Y.H.; Wu, F.Y.; Liu, Z.C.; Chu, Z.Y.; Xie, L.W.; Yang, J.H. Evaluation of Sr chemical purification technique for natural geological samples using common cation-exchange and Sr-specific extraction chromatographic resin prior to MC-ICP-MS or TIMS measurement. *J. Anal. At. Spectrom.* **2012**, *27*, 516. [[CrossRef](#)]
24. Su, A.N.; Tian, S.H.; Li, Z.Z.; Hou, Z.Q.; Hou, K.J.; Hu, W.J.; Gao, Y.G.; Yang, D.; Li, Y.H.; Yang, Z.S. MC-ICP-MS high precision determination of Li isotope analysis method. *Earth Front.* **2011**, *18*, 304–314. (In Chinese with English abstract)
25. Tian, S.H.; Hu, W.J.; Hou, Z.Q.; Mo, X.X.; Yang, Z.S.; Zhao, Y.; Hou, K.J.; Zhu, D.C.; Su, A.N.; Zhang, Z.Q. Mantle source region and petrogenesis of the Miocene Selip superpotassic volcanic rocks in the western part of Lhasa Block: Li isotopic restriction. *Depos. Geol.* **2012**, *31*, 791–812. (In Chinese with English abstract)
26. Tian, S.; Hou, Z.; Mo, X.; Tian, Y.; Zhao, Y.; Hou, K.; Yang, Z.; Hu, W.; Li, X.; Zhang, Y. Lithium isotopic evidence for subduction of the Indian lower crust beneath southern Tibet. *Gondwana Res.* **2020**, *77*, 168–183. [[CrossRef](#)]
27. Millot, R.; Guerrot, C.; Vigier, N. Accurate and high-precision measurement of lithium isotopes in two reference materials by MC ICP-MS. *Geostand. Geoanalytical Res.* **2004**, *28*, 153–159. [[CrossRef](#)]
28. Garth, P.R. Perovskites, niobium perovskites, and Ba-Fe manganites from the Schryburt Lake carbonate complex in northwestern Ontario, Canada. *J. Geosci. Transl.* **1995**, *12*, 1–6.
29. Middlemost, E.A.K. Naming Materials in the Magma/Igneous Rock System. *Earth-Sci. Rev.* **1994**, *37*, 215–224. [[CrossRef](#)]
30. Streckeisen, A. To each plutonic rock its proper name. *Earth-Sci. Rev.* **1976**, *12*, 1–33. [[CrossRef](#)]
31. Middlemost, E. *Magmas and Magmatic Rocks*; Addison-Wesley Longman Ltd.: Boston, MA, USA, 1985.
32. Frost, C.D.; Frost, B.R. On Ferroan (A-Type) Granitoids: Their Compositional Variability and Modes of Origin. *J. Petrol.* **2011**, *52*, 39–53. [[CrossRef](#)]
33. Barth, M.G.; McDonough, W.F.; Rudnick, R.L. Tracking the budget of Nb and Ta in the continental crust. *Chem. Geol.* **2000**, *165*, 197–213. [[CrossRef](#)]
34. Wu, C.B.; Hou, G.S.; Xiang, S.H. Characteristics of Yuchi Syenites from East Qinling and the Rare Metal Elements, Rare Earth Element Mineralization. *Geol. Sci. Technol. Inf.* **2017**, *36*, 58–64. (In Chinese with English abstract)
35. Shi, Y.; Liu, Z.; Liu, Y.; Shi, S.; Wei, M.; Yang, J.; Gao, T. Late Paleozoic-Early Mesozoic southward subduction-closure of the Paleo-Asian Ocean: Proof from geochemistry and geochronology of Early Permian-Late Triassic felsic intrusive rocks from North Liaoning, NE China. *Lithos* **2019**, *346*, 105165. [[CrossRef](#)]
36. Linnen, R.L.; Samson, I.M.; Williams-Jones, A.E. Geochemistry of the Rare-Earth Element, Nb, Ta, Hf and Zr Deposits. In *Treatise on Geochemistry*, 2nd ed.; Holland, H.D., Turekian, K.K., Eds.; Elsevier Science Press: Amsterdam, The Netherlands, 2014; Volume 13, pp. 543–568.
37. Guo, D.X.; Liu, Y. Occurrence and geochemistry of bastnasite in carbonatite-related REE deposit, Mianning-Dechang REE belt, Sichuan Province, SW China. *Ore Geol. Rev.* **2019**, *107*, 266–282. [[CrossRef](#)]
38. Sun, S.S.; McDonough, W.F. *Chemical and Isotopic Systematics of Oceanic Basalts: Implications for Mantle Composition and Processes*; Geological Society, Special Publications: London, UK, 1989; Volume 42, pp. 313–345. [[CrossRef](#)]
39. Hou, Z.; Liu, Y.; Tian, S.; Yang, Z.; Xie, Y. Formation of carbonatite-related giant rare-earth-element deposit by the recycling of marine sediments. *Sci. Rep.* **2015**, *5*, 10231. [[CrossRef](#)]
40. Liu, S.; Fan, H.R.; Yang, K.F.; Hu, F.F.; Rusk, B.; Liu, X.; Li, X.C.; Yang, Z.Y.; Wang, Q.W.; Wang, K.Y. Fertilization in the giant Bayan Obo REE-Nb-Fe deposit: Implication for REE mineralization. *Ore Geol. Rev.* **2018**, *94*, 290–309. [[CrossRef](#)]
41. Zhou, H.S.; Ma, C.Q.; Zhang, C.; Chen, L.; Zhang, J.Y.; She, Z.B. Yanshanian aluminous A-type granitoids in the Chunshui of Biyang, south margin of North China Craton: Implication from petrology, geochronology and geochemistry. *Acta Pet. Sin.* **2008**, *24*, 49–64. (In Chinese with English abstract)
42. Yang, J.H.; Chung, S.L.; Wilde, S.A.; Wu, F.Y.; Chu, M.F.; Lo, C.H.; Fan, H.R. Petrogenesis of postorogenic syenites in the Sulu Orogenic Belt, East China: Geochronological, geochemical and Nd-Sr isotopic evidence. *Chem. Geol.* **2005**, *214*, 99–125. [[CrossRef](#)]
43. Liu, Y.; Chakhmouradian, A.R.; Hou, Z.; Song, W.; Kynický, J. Development of REE mineralization in the giant Maoniuping deposit (Sichuan, China): Insights from mineralogy, fluid inclusions, and trace-element geochemistry. *Miner. Depos.* **2019**, *54*, 701–718. [[CrossRef](#)]
44. Zhao, J.X.; Shiraiishik, A.; Ellis, D.J.; Sheraton, J.W. Geochemical and isotopic studies from the Yamato mountains, East Antarctica: Implication for the origin of syenitic magmas. *Geochim. Cosmochim. Acta* **1995**, *59*, 1363–1385. [[CrossRef](#)]

45. Yang, F.; Pang, X.; Li, B.; Chen, J.; Han, J.; Liu, M.; Yang, Z.; Wang, Y.; Shi, Y. Geological, fluid inclusion, H-O-S-Pb isotope constraints on the genesis of the Erdaogou gold deposit, Liaoning Province. *J. Earth Sci.* **2021**, *32*, 103–115. [[CrossRef](#)]
46. Yan, G.H.; Xu, B.L.; Mu, B.L. Nd, Sr and Pb Isotopic characteristics and significance of Mesozoic alkali-rich intrusions in northern China. *Bull. Mineral. Petrol. Geochem.* **2001**, *20*, 234–236.
47. Ren, K.X.; Yan, G.H.; Cai, J.H.; Mu, B.L.; Li, F.T.; Chu, Z.Y. Nd, Sr and Pb isotopic geochemistry of Paleo-Mesoproterozoic alkaline-rich intrusions from the northern part of the North China Craton: Evidence of the lithospheric mantle enrichment. *Acta Petrol. Sin.* **2006**, *22*, 2933–2944. (In Chinese with English abstract)
48. Ju, N.; Zhang, S.; Bi, Z.W.; Ren, Y.S.; Shi, L.; Zhang, D.; Gu, Y.C.; Sun, Q.S. Geochemical characteristics and geological significance of metallogenic rock bodies of Saima niobium deposit in Fengcheng, Liaoning. *Glob. Geol.* **2019**, *38*, 130–139. (In Chinese with English abstract) [[CrossRef](#)]
49. Zhang, Q.; Wang, Y.; Xiong, X.L.; Li, C.D. *Adakite and Grantie: Challenge and Opportunity*; Chian Land Pres: Beijing, China, 2008; pp. 107–129. (In Chinese with English abstract)
50. Zartman, R.E.; Doe, R. Plumbotectonics—The model. *Tectonophysics* **1981**, *75*, 135–162. [[CrossRef](#)]
51. Zindler, A.; Hart, S.R. Chemical geodynamics. *Annu. Rev. Earth Planet. Sci.* **1986**, *14*, 493–571. [[CrossRef](#)]
52. Williams-Jones, A.E.; Vasyukova, O.V. Niobium, Critical Metal, and Progeny of the Mantle. *Econ. Geol.* **2022**, *118*, 837–855. [[CrossRef](#)]
53. Van Lichtervelde, M.; Holtz, F.; Hanchar, J.M. Solubility of manganotantalite, zircon and hafnon in highly fluxed peralkaline to peraluminous pegmatitic melts. *Contrib. Mineral. Petrol.* **2010**, *160*, 17–32. [[CrossRef](#)]
54. Barnes, E.M.; Weis, D.; Groat, L.A. Significant Li isotope fractionation in geochemically evolved rare element-bearing pegmatites from the Little Nahanni Pegmatite Group, NWT, Canada. *Lithos* **2012**, *132*, 21–36. [[CrossRef](#)]
55. Icenhower, J.; London, D. An experimental study of element partitioning among biotite, muscovite, and coexisting peraluminous silicic melt at 200 MPa (H₂O). *Am. Mineral.* **1995**, *80*, 1229–1251. [[CrossRef](#)]
56. Magna, T.; Novák, M.; Cempírek, J.; Janoušek, V.; Ullmann, C.V.; Wiechert, U. Crystallographic control on lithium isotope fractionation in Archean to Cenozoic lithium-cesium-tantalum pegmatites. *Geology* **2016**, *44*, 655–658. [[CrossRef](#)]
57. Wunder, B.; Meixner, A.; Romer, R.L.; Feenstra, A.; Schettler, G.; Heinrich, W. Lithium isotope fractionation between Li-bearing staurolite, Li-mica and aqueous fluids: An experimental study. *Chem. Geol.* **2007**, *238*, 277–290. [[CrossRef](#)]
58. Sartbaeva, A.; Wells, S.A.; Redfern, S.A.T. Li⁺ ion motion in quartz and β-eucryptite studied by dielectric spectroscopy and atomistic simulations. *J. Phys. Condens. Matter* **2004**, *16*, 8173. [[CrossRef](#)]
59. Maneta, V.; Baker, D.R.; Minarik, W. Evidence for lithium-aluminosilicate supersaturation of pegmatite-forming melts. *Contrib. Mineral. Petrol.* **2015**, *170*, 4. [[CrossRef](#)]
60. Maneta, V.; Baker, D.R. Exploring the effect of lithium on pegmatitic textures: An experimental study. *Am. Mineral.* **2014**, *99*, 1383–1403. [[CrossRef](#)]
61. Weng, Q.; Yang, W.B.; Niu, H.C.; Li, N.B.; Shan, Q.; Fan, G.Q.; Jiang, Z.Y. Two discrete stages of fenitization in the Lizhuang REE deposit, SW China: Implications for REE mineralization. *Ore Geol. Rev.* **2021**, *133*, 104090. [[CrossRef](#)]
62. Li, J.; Huang, X.L.; He, P.L.; Li, W.X.; Yu, Y.; Chen, L. In situ analyses of micas in the Yashan granite, South China: Constraints on magmatic and hydrothermal evolutions of W and Ta–Nb bearing granites. *Ore Geol. Rev.* **2015**, *65*, 793–810. [[CrossRef](#)]

Disclaimer/Publisher’s Note: The statements, opinions and data contained in all publications are solely those of the individual author(s) and contributor(s) and not of MDPI and/or the editor(s). MDPI and/or the editor(s) disclaim responsibility for any injury to people or property resulting from any ideas, methods, instructions or products referred to in the content.